Proceedings of the
Annual Stability Conference
Structural Stability Research Council
St. Louis, Missouri, April 2-5, 2019

Influence of boundary conditions on the shear post-buckling behavior of thin web plates

Peter Wang[1], Kevin Augustyn[2], Alex Gomez[3], Spencer Quiel[4], Maria Garlock[5]

Abstract

Thin steel webs in plate girders possess strength beyond the elastic buckling load which is commonly referred to as the post-buckling capacity. Semi-empirical equations based on experimental tests of plate girders have been used for decades to predict this post-buckling capacity up to the ultimate shear load. However, these predictions are predicated on a specific set of assumptions regarding the boundary conditions of the plate. Specifically, the rotational and translational restraint provided by the stiffeners and flanges are idealized when calculating the post-buckling capacity of the web. To this end, the current design equations provide an approximate (albeit generally conservative) estimate of capacity relative to the test data upon which they are founded. New research by the authors has examined the impact of web boundary conditions on the post-buckling shear capacity. Analyses of isolated web plates, independent of the flanges and stiffeners with idealized boundary conditions, are compared against the response of webs within a plate girder loaded predominantly in shear. Experimentally validated finite element models are the basis for this study. Outputs such as von Mises stresses and principal stresses are examined for the buckled plate, whose behavior is influenced by both membrane stresses and second-order bending effects. These evaluations are performed for a range of panel aspect ratios, axial (longitudinal) restraint, and initial imperfections, with the goal of exploring changes in post-buckling shear capacity as well as changes in the fundamental mechanics. The results of this study have potential implications for current design-basis approaches.

1. Introduction

Shear buckling often governs the design of deep beams in buildings and bridges. Slender plate girders are susceptible to web shear buckling, and these plates have a significant amount of postbuckling shear strength that has been utilized by designers over the past half-century (Skaloud 2013, AISC 2016). However, the true mechanics of this postbuckling shear behavior are yet to be fully understood. More than a dozen proposals have attempted to explain the postbuckling behavior of a plate girder in shear (White and Barker 2008). Virtually all of these proposals have been based on "Tension Field Action" (TFA), where the source of postbuckling strength is the

[1] Graduate Student, Princeton University, <pywang@princeton.edu>
[2] Graduate Student, Lehigh University, <kea217@lehigh.edu>
[3] Graduate Student, Princeton University, <ag19@princeton.edu>
[4] Assistant Professor, Lehigh University, <seq213@lehigh.edu>
[5] Professor, Princeton University, <mgarlock@princeton.edu>

development of tensile stresses along a distinct diagonal called the "tension field." However, several key assumptions of TFA have been proven to be inaccurate by recent research (Yoo and Lee 2006, Glassman and Garlock 2016). A stronger understanding of postbuckling behavior is needed to enable more accurate design equations and more economical plate girder designs. One step towards this goal is to understand the effect of web boundary conditions on shear buckling behavior.

Shear buckling is typically divided into two phases: the elastic regime prior to buckling and the postbuckling regime. Work by early researchers such as Timoshenko and Gere (1961) and Bleich (1952) has thoroughly investigated the elastic shear regime. The elastic shear buckling load V_{cr} is typically calculated using Eq. 1, where k is the shear buckling coefficient, E is the modulus of elasticity, μ is Poisson's ratio, D is the web depth, and t_w is the web thickness.

$$V_{cr} = k\frac{\pi^2 E}{12(1-\mu^2)*(D/t_w)^2}\left(\frac{D}{t_w}\right) \quad (1)$$

Bleich has determined the value of the plate shear buckling coefficient k based on plate aspect ratio and idealized plate boundary conditions (Bleich 1952). Lee et al. (1996) proposed a formula to calculate the k value based flange dimensions. However, the postbuckling behavior has been more elusive to characterize as the plate deviates from its pure shear state due to nonlinear geometric behavior, material plasticity, the development of multi-directional stress fields, and changing roles of the flanges and transverse stiffener. Current research in shear buckling over the past half-century has therefore focused on the postbuckling shear behavior.

Axial and rotational restraint provided to the web by the flange has yet to be incorporated in the simplified and conservative simple-support model used in code (AISC 2016). The flange rotational contribution has not been addressed in either elastic or postbuckling regime in Tension Field Action theory; meanwhile, the flange frame action contribution to strength is only considered in the Eurocode (CEN 2006) and not in the AISC or AASHTO codes (White and Barker 2008). Basler's theory, upon which the US codes are based, conservatively assumes that flanges are infinitely flexible and thus cannot anchor the tension-field (Basler 1961). Lee and Yoo (1999) proposed in their experimental study that the flanges do not anchor the diagonal tensions from the tension field. Yoo and Lee (2006) proposed that the postbuckling reserve (from V_{cr} up to the ultimate shear capacity, V_u) is constant for different flange sizes via computational studies of isolated web panel models.

Few studies have explored the effect of axial (longitudinal) restraint as a boundary condition on shear postbuckling behavior (hereafter called axial restraint). The flanges at the top and bottom of a web panel will add varying amounts of axial restraint at the plate boundary. A concrete slab can add significant axial restraint to a web's freedom of axial translation along its top edge. Bearing supports and other connections may also provide a degree of axial restraint – for deep girders, this restraint is almost always applied eccentric to the girder's neutral axis. Both axially-restrained and axially-free plates have been shown to be in a state of pure shear up to the elastic buckling load (Glassman and Garlock 2016, Garlock et al. 2019, Yoo and Lee 2006). The major differences arise in the postbuckling shear regime.

Different models of axial restraint in the literature have led to different ultimate shear strengths in numerical simulation. Yoo and Lee (2006) have modeled the lower bound of zero axial restraint, leading to predictions that are often lower than the TFA-predicted capacity and experimental tests, especially for smaller aspect ratios. Glassman and Garlock (2016) modeled an upper bound on axial restraint in an isolated web panel and demonstrated good agreement with the V_u of 16 plate girder experimental tests. The true degree of axial restraint offered by the realistic plate girder and the surrounding structure lies somewhere in between the upper and lower bound solutions. To the authors' knowledge, researchers have yet to directly quantify how axial restraint influences postbuckling shear capacity, shear stiffness (load-displacement behavior), and sensitivity to initial imperfection in steel plate girders.

This study investigates the shear postbuckling behavior of slender steel web panels subjected to differing boundary configurations. A detailed finite element study will examine the sensitivity of both isolated panel models and full beam models to axial restraint, panel aspect ratio, discrete modeling of flanges and stiffeners, and initial imperfection. Isolated plate panel models are more convenient due to reduced computational complexity and are generally conservative because of the simply-supported boundary assumption. However, the elastic buckling load, V_{cr}, can be significantly underestimated by neglecting flange rotational restraint (Yoo and Lee 2006, Lee and Yoo 1998). Full beam models can assist in verifying the sensitivity analyses of individual plate panel tests by considering web and flange continuity as well as discrete stiffeners. The comparisons shown in this paper can take the next step toward understanding the postbuckling load path for thin web plates in shear.

2. Plate Girder Prototype

The plate girder prototype for this study is based on Design Example 1 from the *FHWA*'s *Steel Bridge Design Handbook* (Grubb and Schmidt 2012), hereafter referred to as the FHWA 2012 girder. The girder is part of a 3-span continuous bridge design with spans ranging from 42 m (140 ft.) to to 52 m (170 ft.). The girder cross section varies to accommodate positive and negative moment regions; as shown in Fig. 1, the cross section chosen for this study is taken at the location of largest shear with minimum moment. This girder was originally designed as composite with the deck slab and therefore had asymmetric flanges (i.e. a lighter top flange was enabled by continuous bracing against the slab). For simplification, the slab is neglected except for the application of lateral bracing to the top flange. Contributions of the composite slab to the web's postbuckling mechanics will be studied in future phases of this project. As shown in in Fig. 1, the prototype is simplified as symmetric with both flanges having the same dimensions as the larger bottom flanges.

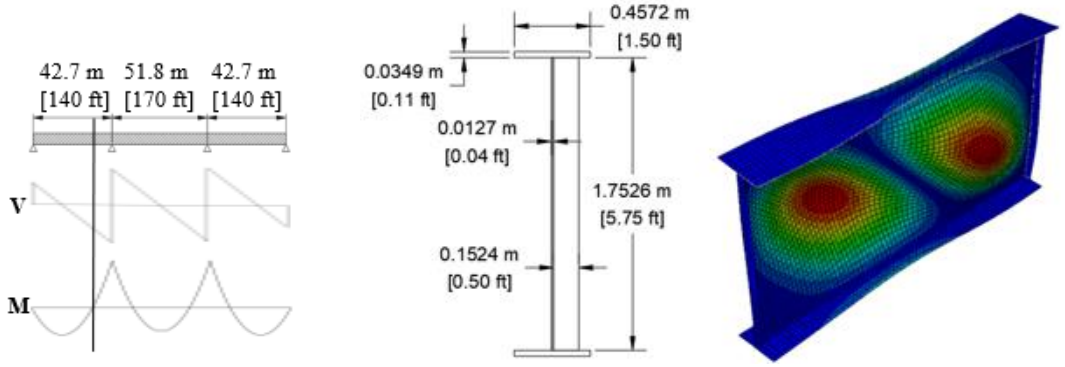

Figure 1: Prototype cross section and typical buckled eigenmode

3. Computational Modeling Approach

The finite element analyses were conducted in the commercial software ABAQUS (Dassault Systemes 2017). Type S4 elements (doubly-curved, general purpose, finite membrane strains) were assigned 4 integration points per quad surface and 5 integration points through the thickness. For each case, an eigenvalue analysis is initially performed to determine the V_{cr} and the shape of the first positive eigenmode, which was scaled to impose an initial imperfection. A quasi-static loading procedure was then performed using a Static-Riks analysis (Glassman and Garlock 2016) to load the plate to failure. The maximum magnitude of this eigenmode imperfection was analzed at both D/10,000 and D/100, where D is the depth of the girder, to examine sensitivity. As shown in Garlock and Glassman (2014), a scaled shape of the first positive eigenmode will allow the simulation to proceed beyond the elastic buckling bifurcation and demonstrate numerically stable postbuckling behavior.

The steel material model was elastoplastic with strain hardening obtained from the Eurocode 3 at ambient temperatures (CEN 2001), with a Young's Modulus of 200 GPa and a Poisson's ratio of 0.3. A von Mises yield criterion with a yield stress of 345 MPa was considered. The nominal stress-strain curve was converted into true stress-strain data for input into ABAQUS. Two types of finite element models are employed: the isolated web panel model and the full beam model.

3.1. Isolated panel models ("P" models)

Isolated panel models are attractive for evaluating shear mechanics due to their computational simplicity. The idealized assumption of a simple supports on all four edges (Fig. 2a) is examined first. Then, the boundary conditions at the top and bottom edges of the web are released and flanges are implemented (F2 model in Fig. 2b). Next, the boundary condition at the vertical edges are released and stiffeners are implemented (F2-S2 model in Fig. 2c).

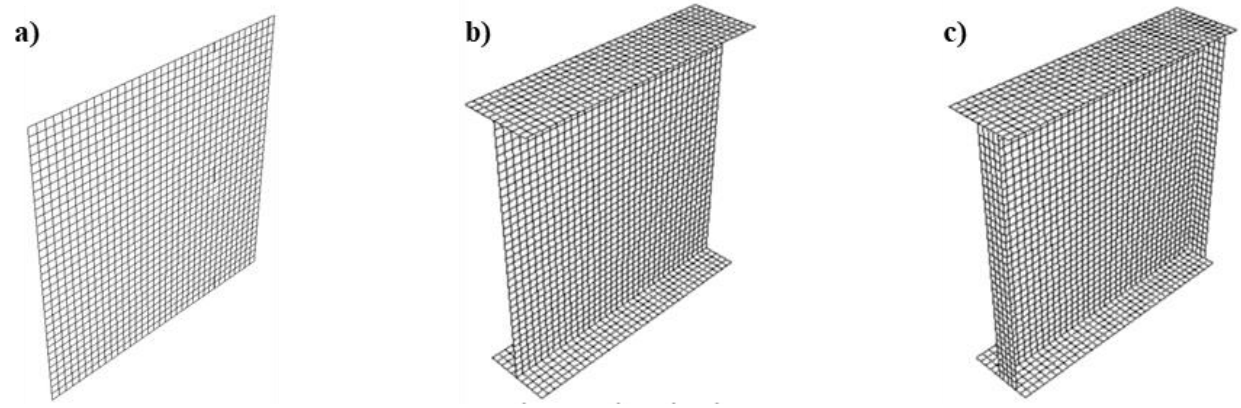

Figure 2: Panel models: a) simply-supported panel, b) panel with flanges, and c) panel with flanges and stiffeners

The boundary conditions used for the simply-supported web panel are given in Fig. 3, along with the loading for pure shear (Garlock et al. 2019). A panel with no restraint of axial translation represents a lower bound (LB). A panel with axial translation restrained on the vertical edges can be considered an upper bound (UB). The mesh density shown in Fig. 3 (35 elements through the depth) was determined through a convergence study. The selected mesh predicted the theoretical elastic buckling load V_{cr} for a simply-supported square panel with less than 1% error versus an eigenvalue analysis.

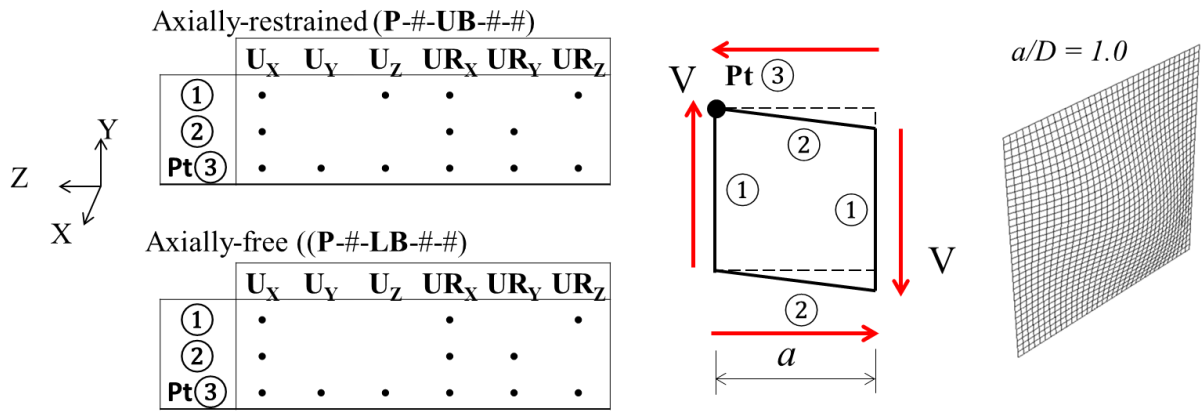

Figure 3: Boundary conditions for isolated panel and mesh density

Panels with flanges used the flange dimensions shown in Fig. 1 (Grubb and Schmidt 2012). Stiffeners were designed to satisfy the postbuckling stiffener moment of inertia requirement per US standards (AASHTO 2007, AISC 2010). To assess the role of the stiffener in providing vertical and rotational restraint to the web panel, all boundary conditions on the vertical web edges were released. No boundary restraints were directly applied to the flanges and stiffeners, and their interfaces with the web and each other were represented with tie constraints to simulate the welds.

3.2. Full beam models ("F" models)

Postbuckling shear results from the isolated plates were compared to full-beam models to examine the influence of realistic boundary conditions and plate continuity. The full beam analysis was performed using the same finite element modeling approach as the panels according to the specifications listed above for the FHWA 2012 girder. The loading and support of the full-beam model is based on the experimental setup used by Hansen (Hansen 2007, 2018) to evaluate the shear buckling behavior of several steel girder specimens. Fig. 4 shows that the full beam representation consists of a critical buckling section (ABCD) and two support sections (EACG and BFHD, which are designed to enforce continuity in the beam but not buckle). The critical section for each model follows the FHWA 2012 girder dimensions for flange and web thickness. The stiffener size was again based on the AASHTO and AISC requirements mentioned above. The length of this section is 4 times the depth of the girder, resulting in 4 panels for the a/D=1 models and 2 panels for the a/D=2 models. In the support section, the web thickness and the thickness of stiffeners 1 and 2 were increased by a factor of 5 in order to resist buckling and enforce plate continuity into the critical section. This section was given a length of 2D to enable to the shear to become uniform at an adequate distance from the discrete support points at F and G.

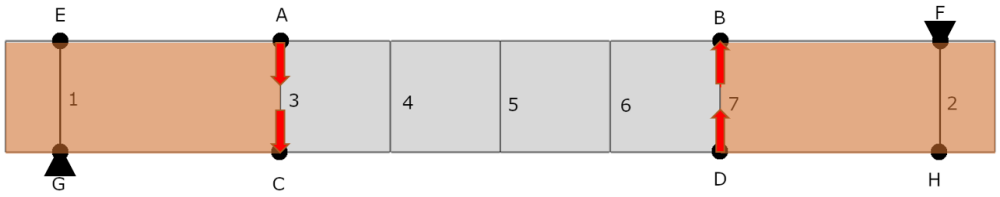

Figure 4: Full beam model (elevation).

The finite element analysis of these models was similarly performed using the Static Riks analysis in ABAQUS (Dassault Systemes 2011). The loading was applied as shown in Fig. 4 with equal value at points A, B, C, and D and increased gradually until failure to avoid localized crumpling at the extents of the critical section. Point G was assigned a pin condition that restrained the flange against translation in all three directions. The support at Point F was modeled as a pin for the upper bound (UB) case and as a roller (i.e. no restraint in the axial direction) for the lower bound (LB) case.

In each analyses, the vertical displacements at A, B, C, and D were incrementally recorded as well as the loads and stresses. The following loading milestones were recorded: load at which the load-displacement curve becomes non-linear (representing V_{cr}), the ultimate load (V_u), the load at which the first plastic hinge forms in the flange (V_h), and the load at which a mechanism forms to collapse the beam (V_m).

3.3. Initial imperfections

Two initial imperfections were examined for both "P" and "F" models to evaluate the sensitivity to different boundary configurations. The lower bound initial imperfection had a magnitude of D/10,000 of the first positive buckled eigenmode, where D is the depth of the girder web (corresponding to a ~0.2-mm magnitude imperfection for the prototype). The upper bound was an initial imperfection magnitude of D/100 (corresponding to a ~2-cm magnitude imperfection for the prototype), which is the maximum initial imperfection allowed by the American Welding Society (AWS) in the Bridge Welding Code (Yoo and Lee 2006). Similarly, the Eurocode (CEN 2006) recommends an equivalent geometric imperfection of magnitude D/200 of the first positive buckled eigenmode to model the effect of weld-based residual stresses and geometrical imperfections on shear behavior.

4. Results

An eigenvalue analysis and subsequent Static Riks failure analysis was conducted for each boundary configuration model. The elastic shear buckling load (V_{cr}) and the ultimate shear load (V_u) for each case are summarized in Table 1. For each model, the ratio of V_u/V_{cr} and a measure of the additional shear strength beyond elastic buckling (the postbuckling reserve V_u - V_{cr}) is also shown. Boundary configurations are noted using the following nomenclature. The first letter in each run denotes a full beam model (F) or isolated panel (P). The second index lists the web panel a/D ratio (1 or 2). The third index indicates the axial restraint in the plate (UB = fully restrained, LB = no restraint). If the flange is modeled, an "F2" index is present. If the stiffener is modeled, "S2" is added. Lastly, the initial imperfection magnitude is indicated by I1 (D/10,000) or I2 (D/100). Note that the model for the a/D = 2 panel with axial restraint and an initial imperfection of D/100 did not obtain a failure mechanism due to numerical non-convergence but successfully reached all other milestones in the analysis. All other cases achieved full numerical convergence to the formation of a failure mechanism.

Table 1: Matrix of analysis cases and results

Panel a/D = 1	V_{cr} (kN)	V_u (kN)	V_u /V_{cr}	V_u - V_{cr} (kN)	V_u I1 / I2	V_u / TFA
P-1-UB-I1	1983	3580	1.81	1597	1.01	0.98
P-1-UB-I2	1983	3557	1.79	1573		0.97
P-1-LB-I1	1982	2596	1.31	614	1.10	0.71
P-1-LB-I2	1982	2351	1.19	369		0.64
P-1-LB-F2-I1	2596	3076	1.18	480	1.15	0.84
P-1-LB-F2-I2	2596	2682	1.03	86		0.73
P-1-UB-F2-S2-I1	2716	3666	1.35	950	1.02	1.00
P-1-UB-F2-S2-I2	2716	3605	1.33	889		0.99
P-1-LB-F2-S2-I1	2714	3202	1.17	487	1.14	0.88
P-1-LB-F2-S2-I2	2714	2799	1.03	84		0.77

Panel a/D = 2	V_{cr} (kN)	V_u (kN)	V_u /V_{cr}	V_u - V_{cr} (kN)	V_u I1 / I2	V_u / TFA
P-2-UB-I1	1391	2642	1.90	1251	1.00	1.02
P-2-UB-I2	1391	2649	1.91	1259		1.02
P-2-LB-I1	1389	2071	1.49	682	1.06	0.80
P-2-LB-I2	1389	1952	1.41	563		0.75
P-2-LB-F2-I1	2004	2724	1.36	720	1.14	1.05
P-2-LB-F2-I2	2004	2391	1.19	388		0.92
P-2-UB-F2-S2-I1	2025	3080	1.52	1055	1.04	1.18
P-2-UB-F2-S2-I2	2025	2963	1.46	939		1.14
P-2-LB-F2-S2-I1	2025	2756	1.36	732	1.12	1.06
P-2-LB-F2-S2-I2	2025	2461	1.22	436		0.95

a/D = 1 girder panel: TFA capacity is 3649 kN
a/D = 2 girder panel: TFA capacity is 2601 kN

FULL BEAM 1	V_{cr} (kN)	V_u (kN)	V_u /V_{cr}	V_u - V_{cr} (kN)	V_u I1 / I2	V_u / TFA	V_h (kN)	V_m (kN)
F-1-UB-F2-S2-I1	1769	3133	1.77	1364	1.00	0.86	2841	3057
F-1-UB-F2-S2-I2	1769	3118	1.76	1349		0.85	2993	3098
F-1-LB-F2-S2-I1	2216	3187	1.44	971	1.01	0.87	2856	3143
F-1-LB-F2-S2-I2	2216	3154	1.42	938		0.86	2867	3141
F-2-UB-F2-S2-I1	1511	2990	1.98	1479	1.00	1.15	2954	2776
F-2-UB-F2-S2-I2	1511	2993	1.98	1482		1.15	2941	N/A
F-2-LB-F2-S2-I1	1818	2892	1.59	1074	1.02	1.11	2845	2469
F-2-LB-F2-S2-I2	1818	2824	1.55	1006		1.09	2824	2431

The results for ultimate shear strength are compared with TFA estimates. Lee and Yoo (1998) showed that TFA predictions agree relatively well with experimental tests for a/D ≤ 1.5 but are increasingly conservative at a/D ratios approaching 3.0. The P-#-UB- models corresponded well with the TFA ultimate strength predictions for both a/D = 1 and 2. The lower bound P-#-LB- models tended to fall well below TFA capacity (by ~30% for P-1-LB-I1). However, as more girder components were discretely modeled, the underestimation of the ultimate strength reduced. In particular, the P-1-UB-F2-S2 models (with flanges and stiffeners) included agreed within 1% of TFA estimates. Model predictions were under TFA predictions at a/D = 1 but produced mixed predictions for a/D = 2. This relation with TFA predictions agrees with the trends observed from previous experimental studies (Lee and Yoo 1998). The full beam models also agreed relatively well with TFA predictions, with a/D = 1 cases ~15% lower and a/D = 2 cases ~15% greater. The smaller D/10,000 imperfections produced up to 15% greater V_u than the larger D/100 imperfections, with the P-#-UB- models and all full beam models showing very little difference (less than 5%) between the two.

4.1. Strength Comparison: Panel to Full Beam

Table 2 summarizes the variation in values of V_{cr} and V_u between the panel and full beam models for each boundary configuration. The V_u of case 1-LB-F2-S2-I1 (axially-free with a/D = 1 and D/10,000 initial imperfection) showed the best agreement between the isolated panel and full beam models, differing by only +0.5%. The axially-restrained version for the panel produced 15% larger V_u for a/D = 1 than the full beam due to the closer proximity of its restrained boundary condition to the buckled section. The full beam models showed lower V_{cr} for all cases, up to 42% lower for cases with a/D = 1 and UB axial restraint, due to their added flexibility and non-ideal boundary conditions.

Table 2: Comparison of panel and full beam model results.

Comparison of Panel (P) and Full Beam (F)	**% Difference**	
Model	V_{cr}	V_u
[F or P]-1-LB-F2-S2-I1	+20 %	+0.5 %
[F or P]-1-LB-F2-S2-I2	+20 %	-12.0%
[F or P]-1-UB-F2-S2-I1	+42 %	+15.7 %
[F or P]-1-UB-F2-S2-I2	+42 %	+14.5 %
[F or P]-2-LB-F2-S2-I1	+11 %	-4.8 %
[F or P]-2-LB-F2-S2-I2	+11 %	-13.7 %
[F or P]-2-UB-F2-S2-I1	+29 %	+3.0 %
[F or P]-2-UB-F2-S2-I1	+29%	-1.0%

*positive % difference corresponds to a higher shear value from the isolated panel models.

The increase in initial imperfection had a negligible effect on V_u for models with axial restraint (UB) for both isolated panel and full beam (UB) cases, agreeing well in their sensitivity. However, the increase in initial imperfection yielded a large 10-14% reduction in V_u in the isolated panel models with no axial restraint (axially free plates). In addition, the effect on V_u of increasing the

initial imperfection was magnified when flanges and/or stiffeners were discretely modeled in the isolated panel. The axially-free full beam models (e.g. F-1-LB-F2-I2 and F-2-LB-F2-I2) also demonstrated slightly larger sensitivity to initial imperfection than the restrained case, with a 1-2% reduction in ultimate strength due to the D/100 imperfection.

Overall, though not as significant as that in the isolated panel models, the effect of the change in the initial imperfection from D/10,000 to D/100 causes a decrease in V_u ranging from 20 to 70 kN, which accounts for only about 2% of the strength of the full beams. This indicates that the beam models are overall not as sensitive to the imperfection changes. By increasing the initial imperfection, there is a large reduction in shear stiffness among all isolated panel models, as illustrated in the load vs. vertical displacement curves of Fig. 5. The buckling bifurcation V_{cr} in the load-displacement curve is less visible for larger D/100 initial imperfection, as second order-bending effects soften the onset of buckling. The plots of maximum out-of-plane web displacement in Fig. 6 confirm that the D/100 imperfection allows much more "bulging" of the plate throughout the application of shear, even well before buckling would be expected. The reduction in shear stiffness is much less significant for the full beam models, as observed in Fig. 7 and 8.

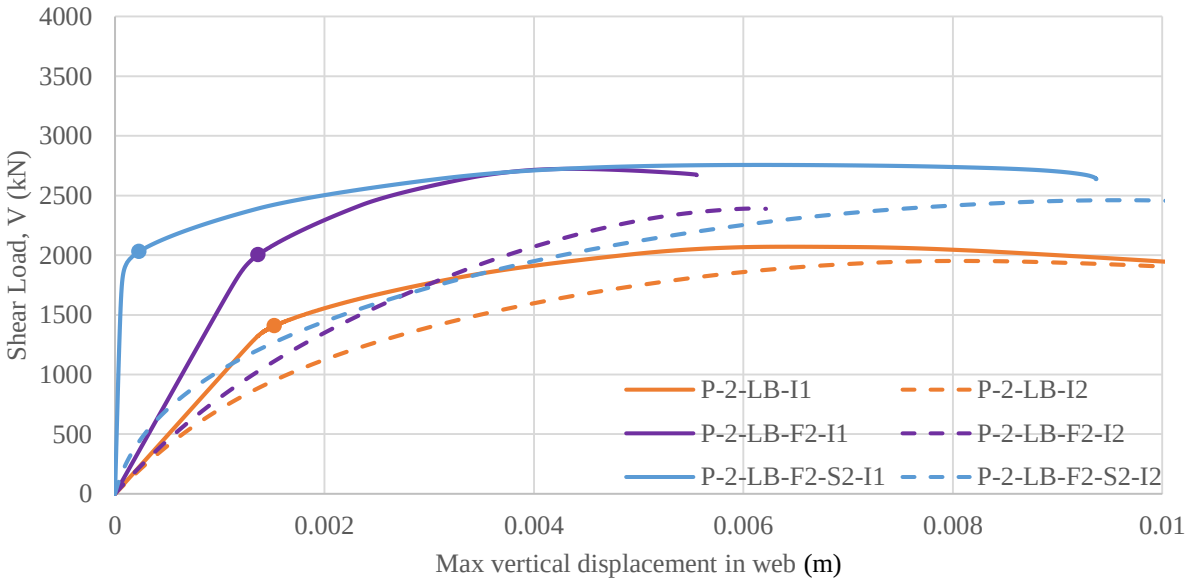

Figure 5: Load vs. vertical displacement for the axially-free panels, a/D = 2. The circles denote V_{cr} for each curve.

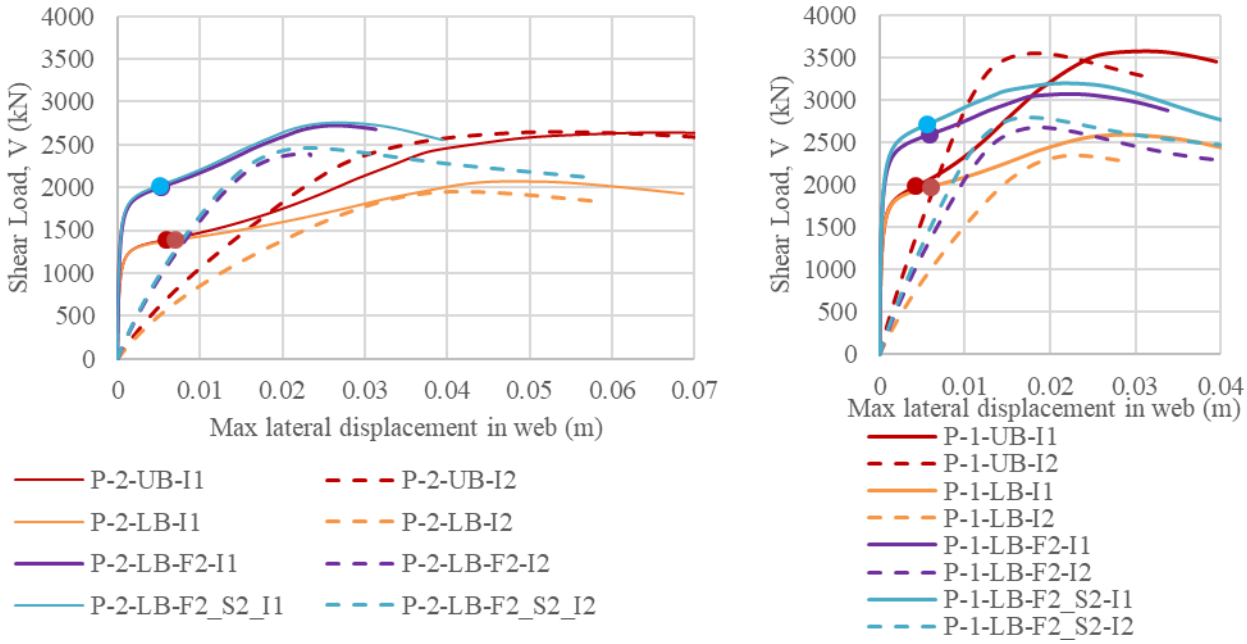

Figure 6: Load vs. lateral displacement for the isolated panels: a/D = 2 (left) and a/D = 1 (right).

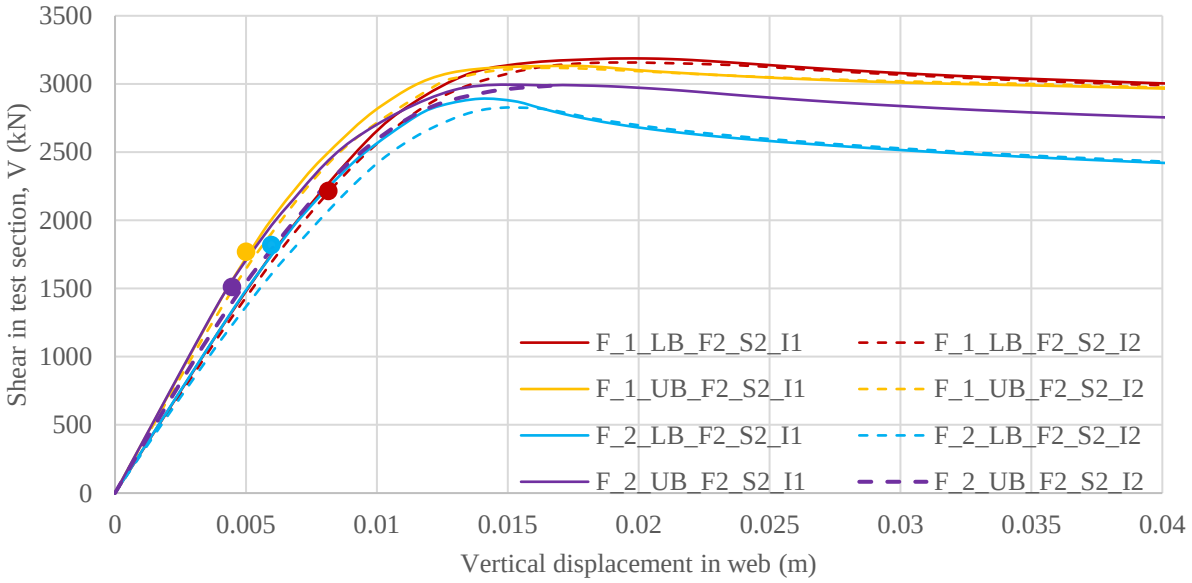

Figure 7: Load vs. vertical displacement at point A (see Fig. 4) of the full beam model

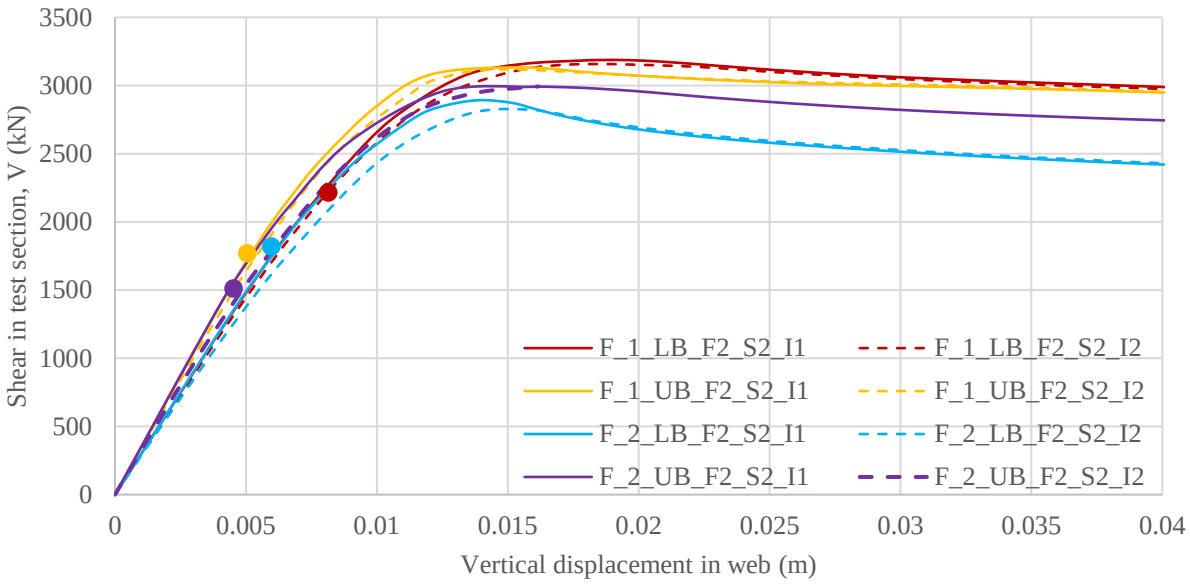

Figure 8: Load vs. vertical displacement at point B (see Fig. 4) of the full beam model

4.2. Effects of axial restraint:

The corresponding P-#-UB- and P-#-LB- models experienced the same V_{cr} since both axially-restrained (UB) and axially-free (LB) conditions subject the plate panel to pure shear prior to buckling. However, the ultimate postbuckling strength V_u (and therefore the postbuckling reserve) was found to be largely dependent on the axial restraint in the plate. This shows that the degree of axial restraint is especially important in the postbuckling behavior. By observing the load vs. lateral deflection curves from Fig. 6, the LB models experience higher out-of-plane deformation at lower loads, showing that they crumple faster after V_{cr}, which may reduce their postbuckling strength. For the a/D = 1 simply-supported plate panel, the V_u with axial restraint was 38% greater than the axially-free plate (1-UB-I1 vs. 1-LB-I1, respectively), while for a/D = 2 the difference was 28% (2-UB-I1 vs. 2-LB-I1). The effect of axial restraint is therefore magnified when the axial restraints are placed closer to each other (as in the a/D = 1 panel).

When axial restraint is present in the isolated panels, the closer case is a pin-pin condition in the full-beam test setup (though in this case, the locations of axial restraint are placed much farther away from each other, separated by both longitudinal distance and depth). There is no clear bifurcation in the load-displacement curve at the elastic buckling load in either case (see Fig. 7 and 8). Instead, the loss in stiffness is gradual following elastic buckling.

When the panels are axially-free (e.g. P-2-LB-F2-S2-I1), the analogous case is a pin-roller condition in the full-beam tests (F-2-LB-F2-S2-I1). For these cases, there is typically a clear bifurcation (change in slope) in the load vs. vertical displacement curve at the elastic buckling load, as illustrated in Fig. 5 for a/D = 2 panels. The bifurcation in the load-displacement curve is clearly demarcated by a circular marker at V_{cr} for all three axially-free plates shown. The clarity of the buckling bifurcation goes away when the degree of initial imperfection is raised to D/100 in the I2 models. A similar trend exists for the axially-free full beam models.

The full beam saw significant differences in the eigenvalues (V_{cr}) based upon the axial restraint.

The initial buckling occurred much earlier in the axially-restrained beams than the axially-free (LB) ones. There were minor differences, up to 5.6%, in V_u based upon this factor, indicating that the axially restrained beams displayed much more post-buckling reserve than the non-restrained ones. The observed phenomenon is a result of far-end restraint and eigenmode differences. The axially-restrained beam will favor nearly symmetric eigenmodes, which will cause buckling more quickly but will be distributed more evenly throughout the beam. The unrestrained beam favors the pinned side much more in the eigenvalue analysis, and the rest of the beam therefore retains resistance longer before buckling. This can be seen in the load-deflection curves in Figs. 7 and 8 which show that the post-V_{cr} displacement to V_u for the axially restrained beams is larger than for the non-axially restrained ones. These findings regarding the larger postbuckling reserve for the axially-restrained beam agrees well with the findings from the isolated panels.

4.3. Influence of discrete flange and stiffeners

By comparing models P-2-LB-I1, P-2-LB-F2-I1, and P-2-LB-F2-S2-I1, it is seen that the elastic buckling load V_{cr} grows progressively as more physical components are added in lieu of idealized boundary conditions (as was also shown by Lee and Yoo 1998). The elastic shear stiffness (vertical stiffness) and V_u are also increased when the flange and stiffener are explicitly modeled (see Fig. 5).

For the full beam models, the shear load at the onset of flange hinging (V_h) stays nearly constant through all of the models, varying by less than 5%. This indicates a low sensitivity of this mechanical milestone to the a/D ratio, axial restraint, and initial imperfection. In addition, the flange mechanism load V_m always occurs after the ultimate shear V_u is reached. This finding suggests that the flanges take on more of the load via flange frame action only after the web has been compromised. Values for V_m follow a very similar pattern to V_u and are sensitive to the axial restraint and panel aspect ratio.

4.4. von Mises stress analysis

The von Mises stresses are used to compare overall stress distributions between different panel and full beam models. Fig. 9 shows the von Mises stresses plotted for P-1-UB-I1, P-1-LB-F2-S2-I1, P-1-LB-F2-S2-I2 and F-1-LB-F2-S2-I2 (taking the web panel in the center-right of the full beam model). For each specimen, the stresses are plotted at the top and bottom web plate surfaces as well as at the center of thickness. The grey shading represents yielding in the plate.

The von Mises stresses in the full beam test section F-1-LB-F2-S2-I2 (in the area of high shear and minimum moment) agrees well with the von Mises stress distributions of the isolated panels, as shown for the a/D = 1 model without axial restraint (P-1-LB-F2-S2-I1, P-1-LB-F2-S2-I2). Note that the shear on the F-model is acting in opposite direction to the shear on the P-model. For each of the models shown in Figure 9, the von Mises stresses vary across the three plate planes shown (from bottom surface to center of thickness to top surface). This implies that bending stresses exist at the ultimate postbuckling shear load V_u.

At the ultimate load V_u, through-section yielding occurs on the tension diagonal when there is axial restraint in the plate (P-1-UB-I1). However, when the axial restraint is released there is no von Mises yielding in the center of thickness (P-1-LB-F2-S2-I1 and P-1-LB-F2-S2-I2), only on the plate surfaces. No through-section yielding occurs in the full beam model (F-1-LB-F2-S2-I2)

either. This yielding behavior through the depth of the thickness likely plays a role in the development of V_u.

The plots for P-1-LB-F2-S2-I1 and P-1-LB-F2-S2-I2 are compared to view the effect of initial imperfection magnitude on stress distribution (Fig. 9). The stress pattern for both models is the same but the larger initial imperfection of D/100 results in slightly more von Mises yield at V_u. This observation is likely related to the larger V_u for the D/100 model compared to the D/10000 model (3202 kN vs 2799 kN).

4.5. Principal membrane stress analysis

The principal membrane stresses are independent of bending effects and thus enable one to investigate the load path and flow of forces through the web panel. Membrane stresses are equal to the membrane forces divided by the plate thickness. Garlock et al. (2019) have performed an initial analysis on an axially-restrained plate. In this paper, different boundary conditions are considered: an axially restrained plate, an axially-free plate, and an axially-free plate with flanges and stiffeners. Analyses are made for plates of a/D = 1; however, results for a/D = 2 are similar.

To analyze traditional shear load paths, the compression diagonal is first analyzed (shown shaded in the inset figure of Fig. 10). Many previous papers (Glassman and Garlock 2016, Yoo and Lee 2006) have focused on the state of stresses at the elastic shear buckling load and at the ultimate shear load; however, this paper explores the load history to give a more continuous sense of the postbuckling mechanics. Tension Field Action (TFA) theory posits that after the elastic shear buckling load, compressive stresses cease to increase and all additional load is taken by the tension field (increased tensile membrane stresses only). Garlock et al. (2019) showed that this was not the case for an axially-restrained plate by investigating the load history.

Figure 10 plots the minimum principal membrane stress (i.e. the compressive membrane stress) for each element along the compression diagonal. Green curves are for elements with a compressive membrane stress greater than the elastic buckling stress τ_{cr} at the ultimate load V_u, while orange curves are for elements at compressive stress less than τ_{cr} at V_u. Similar to what is shown in Garlock et al. (2019), compressive membrane stresses increase beyond τ_{cr} across the entire compression diagonal until more than half (67%) of the postbuckling reserve (additional strength beyond V_{cr}) has been achieved. The intermediate shear load (V_i) represents the load up to which compression membrane stresses continue to increase throughout the plate. In addition, compressive membrane stresses farther from the plate center (around the plate perimeter) are shown to increase at a uniform rate up to the ultimate shear load V_u, similar to the rate of stress increase before buckling. While some compressive membrane stresses are at or lower than the elastic buckling stress τ_{cr} at the ultimate shear load V_u, Fig. 10 shows that they increase beyond the elastic buckling load V_{cr} before decreasing prior to failure.

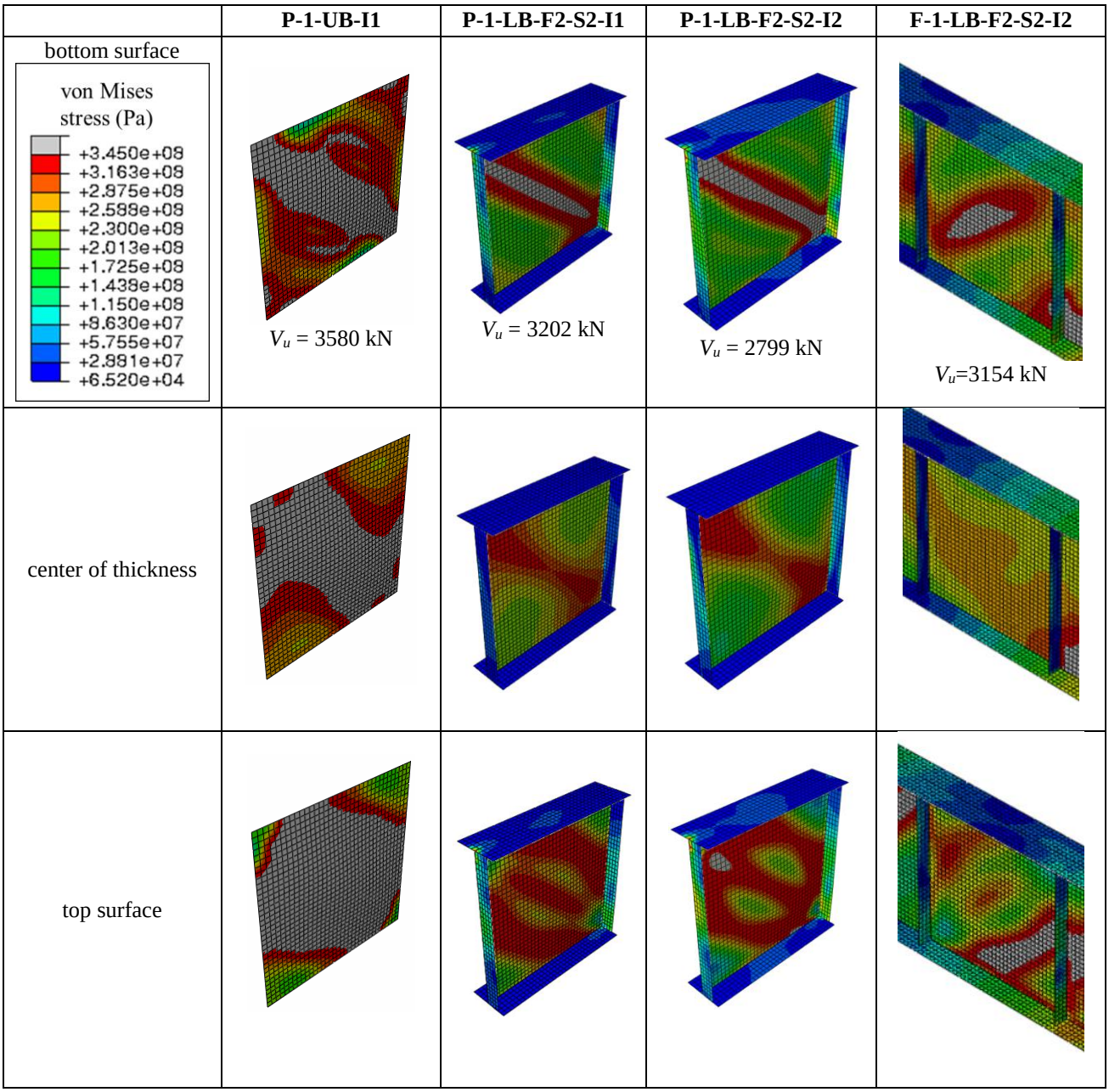

Figure 9: von Mises stress distributions at the bottom surface, center of thickness, and top surface of each web plate. Gray denotes regions of yield. All stresses shown are in Pa.

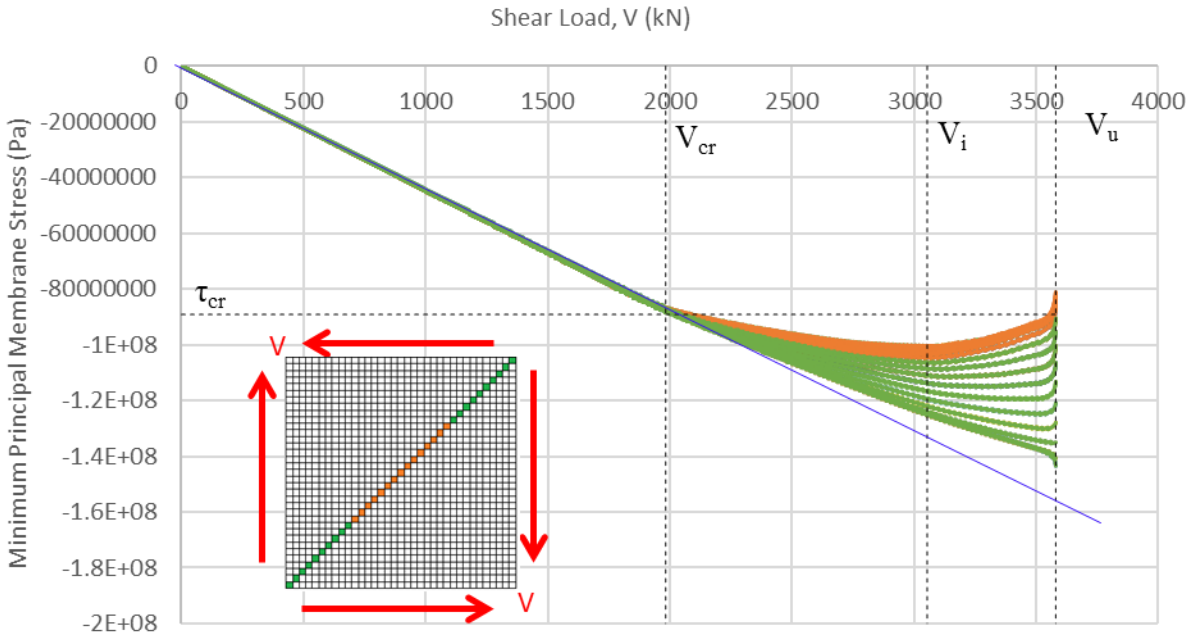

(a)

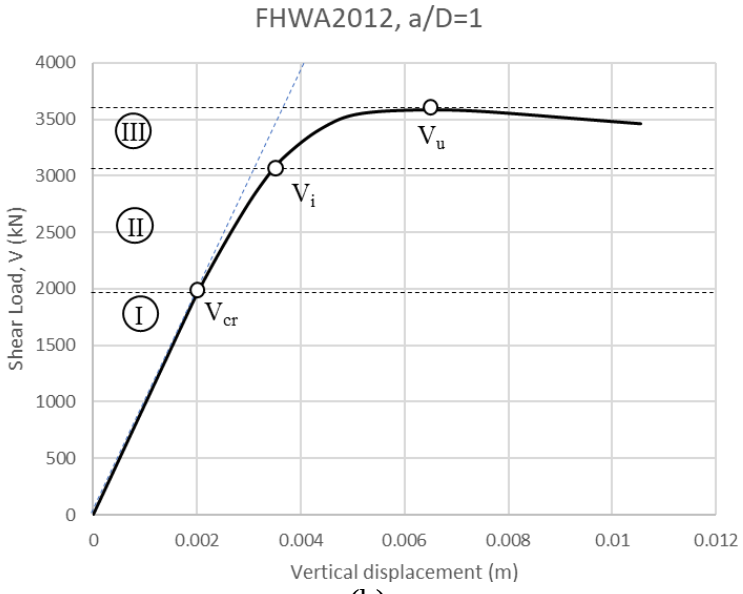

(b)

Figure 10: P-1-UB-I1 (a) compressive stress vs. load applied to elements on the compression field diagonal (shaded in inset figure), (b) Zones I, II and III on load vs. vertical displacement plot

Figure 11 is similar to Figure 10 except that it is for an axially-free web plate (Model 1-LB-I1). Though there is less restraint afforded against crumpling of the plate, a similar phenomenon is observed. Fig. 11(a) shows that compression membrane stresses increase across the entire compression diagonal until more than half (55%) of the postbuckling reserve is achieved, regardless of axial restraint in the plate. (This is alternatively shown by Zone II in the load-displacement graph [Fig. 11(b)].) This result demonstrates that axial restraint on the plate is not necessary for postbuckling compressive stresses to develop; a lower-bound model without flanges or slab can develop increasing postbuckling compressive stresses (though the extent of the

compressive stress increases beyond V_{cr} is reduced for elements near the plate center when compared to the axially-restrained plate).

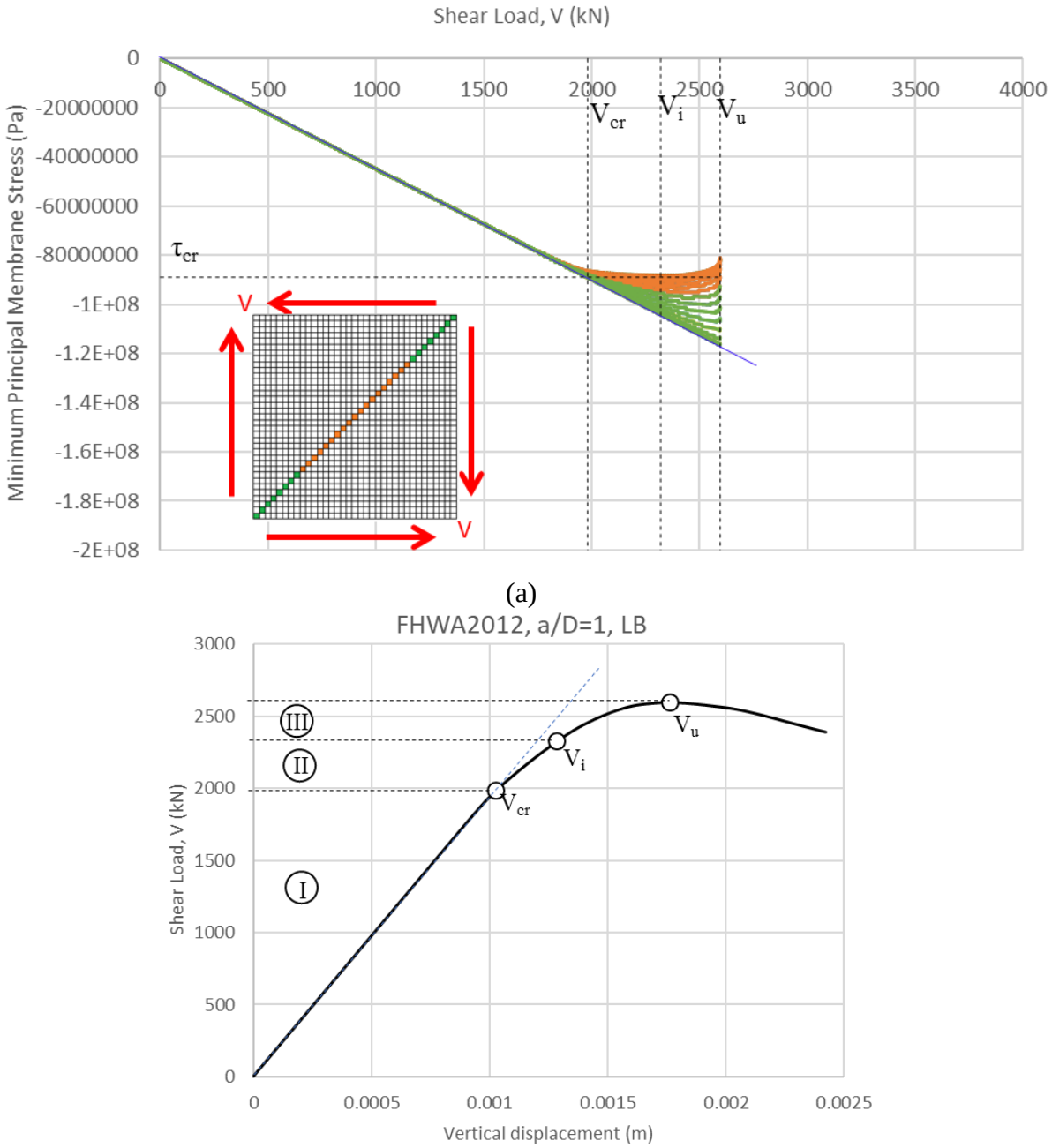

Figure 11: P-1-LB-I1 (a) compressive membrane stress vs. load applied to elements on the compression field diagonal (shaded in inset figure), (b) Zones I, II and III on load vs. vertical displacement plot

Although not shown, similar studies were done with the plate with flanges and stiffeners for boundary conditions (P-1-LB-F2-S2-I1). The results are similar. The main difference in the behavior is that: 1) the rate of compressive stress increase is pushed forward to a higher elastic shear buckling load V_{cr}, as noted by Lee and Yoo (1996, 1998); and 2) there are fewer elements along the compression diagonal that are above the elastic buckling stress τ_{cr} at the failure load. Note

that the compressive membrane stress still increase after reaching V_{cr}, but they decreased shortly prior to failure.

Yoo and Lee (2006) and Garlock et al. (2019) have shown the potential importance of compressive membrane stresses along the perimeter of the plate, which Garlock et al. (2019) have shown to continue to increase at a rate similar to the rate of compressive stress increase prior to elastic shear buckling. An analogous study is taken to view the compressive membrane stress behavior along the opposite (tension field) diagonal, where the compression load path is less disturbed by the out-of-plane bifurcation. Fig. 12 shows the results of the same analysis conducted on the tension diagonal for the axially-free plate with flanges and stiffeners. The graph appears analogous to the graph for elements on the compression diagonal, with a key difference. The blue "elastic line" denotes the rate of compressive stress increase before elastic buckling. It appears that certain elements that are near the perimeter of the plate have compressive membrane stresses that are mirrored across the blue line; meaning that compressive membrane stresses increase at a greater rate for these elements after elastic buckling. Though not pictured, the same phenomenon occurs with the axially-free plate without flanges and stiffeners (P-1-LB-I1). This points to a redistribution of the load path towards compression in the perimeter elements. Further, the tensile principal membrane stresses of these same perimeter elements are significantly less than the compressive membrane stresses at ultimate shear load V_u.

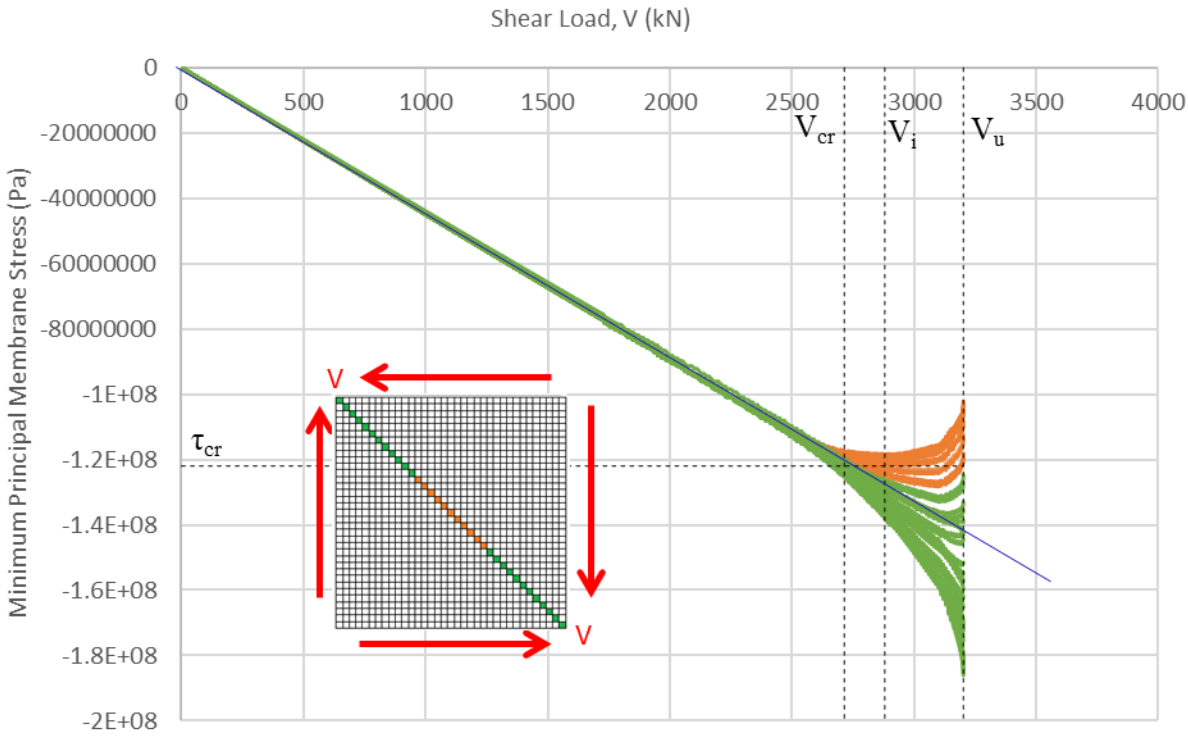

Figure 12: P-1-LB-F2-S2-I1 compressive membrane stress vs. load applied to elements on tension field diagonal (shaded in inset figure)

5. Conclusions

This paper evaluated the shear postbuckling behavior of slender steel web panels subjected to differing boundary configurations as represented by: (1) isolated panel models vs. full beam

models; (2) axial restraint in the longitudinal direction; and (3) discrete modeling of flanges and stiffeners vs. idealized boundary conditions. The effects of panel aspect ratio and initial imperfection were also examined. The elastic shear buckling load V_{cr}, and the ultimate shear postbuckling load V_u were evaluated for these different parameters as well as the load path. The results indicated the following:

- *Isolated panels vs. full beam models:* The prediction of V_{cr} was significantly larger for panel models. The prediction of V_u agreed to within 16%. The stress distributions were similar for both models.
- *Axial restraint:* The shear postbuckling behavior was found to be sensitive to the degree of axial restraint in a girder panel. The additional shear capacity beyond elastic buckling ($V_u - V_{cr}$) was significantly larger for panels with axial restraint.
- *Initial imperfection:* For the single panel models, axially-free boundary conditions were found to be more sensitive to initial imperfection than axially-restrained panels in terms of V_u; however, in the full beam models, where the locations of axial restraint were placed farther from each other, the difference in sensitivity diminished. The effects of initial imperfections on V_u were similar for the different panel aspect ratios tested.
- *Load path:* Examination of compressive stresses along the two 'diagonal cuts' of the plate (i.e., the compression path and tension path) indicated that the compressive stresses continue to increase beyond V_{cr} for both axially-restrained and axially-free plates. Additionally, the compressive stresses indicated a change in load path and movement towards the perimeter elements (i.e., towards the corners).

6. Acknowledgments

This research was sponsored by the National Science Foundation (NSF) under grants CMMI-1662886 and CMMI-1662964. All opinions expressed in this paper are the authors' and do not necessarily reflect the policies and views of the sponsors.

7. References

AASHTO. (2007). AASHTO LRFD Bridge Design Specifications. American Association of State Highway and Transportation Officials.

AISC (2016). Specification for Structural Steel Buildings. American Institute of Steel Construction, Chicago, IL.

Bleich, F. (1952). Buckling Strength of Metal Structures. McGraw Hill, New York.

Dassault Systemes (2011). "ABAQUS 6.11ef Online Documentation." (Nov. 2018).

CEN. (2006). EN 1993-1-5:2006 (E) Eurocode 3: Design of steel structures – Part 1-5: General rules - Plated structural elements. The European Union.

CEN. (2001). Eurocode 3: Design of steel structures: Part 1.2 General rules – Structural fire design. The European Union. BSI, London.

Garlock, M.E.M., and Glassman, J.D. (2014). "Elevated temperature evaluation of an existing steel web shear buckling analytical model." Journal of Constructional Steel Research, 101, 395-406.

Garlock, M.E.M, Quiel, S.E., Wang, P.Y., Alos Moya, J., Glassman, J.D. (2019). "Postbuckling Mechanics of a Square Slender Steel Plate in Pure Shear." Engineering Journal, American Institute of Steel Construction, 56(1), 27-46.

Glassman, J. D., and Garlock, M. E. M. (2016). "A Compression Model for Ultimate Postbuckling Shear Strength." Thin-Walled Structures, 102, 258-272.

Grubb, M. A., and Schmidt, R.P. (2012). "Design Example 1: Three-Span Continuous Straight Composite Steel I-Girder Bridge," Steel Bridge Design Handbook. FHWA-IF-12-052, 20.

Basler, K. (1961). "Strength of Plate Girders in Shear." Trans. ASCE, 128(2).

Basler, K., Yen, B., and Mueller, J. (1960). "Web Buckling Tests on Welded Plate Girders." Welding Research Council, 64.

Lee, S. C., Davidson, J. S., and Yoo, C. H. (1996). "Shear buckling coefficients of plate girder web panels." Computational Struct., 59(5), 789-795.
Lee, S.C., and Yoo, C.H. (1999). “Experimental Study on Ultimate Shear Strength of Web Panels.” Journal of Structural Engineering, 125(8), 838-846.
Hansen, T. (2007). “Theory of Plasticity for Steel Structures: Solutions for Fillet Welds, Plate Girders and Thin Plates.” BYG-Rapport, R-146.
Hansen, T. (2018). "Post-buckling strength of plate girders subjected to shear - experimental verification." Steel Construction, 1-8.
Skaloud, M. (2013). "Breathing-induced fatigue in thin-walled construction." Procedia Engineering, 66, 383-392.
Timoshenko, S. P., and Gere, J. M. (1961). Theory of Elastic Stability, McGraw-Hill, Toronto.
White, D. W., and Barker, M. G. (2008). "Shear Resistance of Transversely Stiffened Steel I-Girders." Journal of Structural Engineering, 134(9), 1437-1449.
Yoo, C. and Lee, S. (2006). "Mechanics of Web Panel Postbuckling Behavior in Shear." Journal of Structural Engineering, 132(1), 1580-1589.